Currentless reversal of Néel vector in antiferromagnets

Yuriy G. Semenov,[1] Xi-Lai Li,[1] and Ki Wook Kim[1,2,*]

[1]*Department of Electrical and Computer Engineering, North Carolina State University, Raleigh, North Carolina 27695, USA*
[2]*Department of Physics, North Carolina State University, Raleigh, North Carolina 27695, USA*

The possibility of magnetization reversal via a bias-mediated perpendicular magnetic anisotropy is examined theoretically in an antiferromagnet. The numerical analyses based on a Néel vector formulation as well as the micromagnetic Landau-Lifshitz-Gilbert simulation reveal that the desired switching can be achieved through dynamical responses that are significantly different from their ferromagnetic counterparts. Instead of the usual precessional trajectories around the applied effective magnetic field, their motions are rather pendulum-like due to the layered magnetic sublattices with a strong antiparallel exchange interaction, where the inertial behavior plays a crucial role. The absence of spiral damping can also lead to faster relaxation by orders of magnitude. With no reliance on the current driven processes, the investigated mechanism is predicted with a low energy requirement of only a few aJ per switching operation in the antiferromagnets.

I. INTRODUCTION

In the early stages of spintronics, antiferromagnets (AFMs) were exploited almost exclusively in combination with free ferromagnetic layers. The primary driver is the large magnetoresistance at these interfaces (i.e., the so-called giant magnetoresistance), which has since played a significant role in the development of numerous applications, such as magnetic random access memory [1,2]. Only recently have they been recognized as an active spintronic medium with excellent dynamical properties that can in fact claim advantages over their conventional ferromagnetic counterparts [3–5]. Similarly to ferromagnets (FMs), AFMs possess two quasistable states along the easy axis that provide a natural system to encode or store the binary information—the logical bit. However, the absence (or near absence) of net magnetization can make its manipulation nontrivial, particularly with external magnetic fields. An alternative approach for control is to take advantage of the "effective" field or torque induced via the magnetic interactions with adjacent layers whose materials are not necessarily magnets [6,7].

One solution proposed earlier is in the manner of spin-transfer torque in FMs exploiting the dynamical origin of AFM magnetization [5,8–10]. However, the current density needed to generate sufficient torque remains high even for AFMs [5]. Further, the weak magnetization tends to extend the transverse electron spin decoherence length, requiring a thicker layer for the AFMs to rely on the Slonczewski's mechanism of spin-transfer torque [11]. Other current driven approaches such as spin-orbit torques and staggered spin-orbital fields appear to require similarly high current densities [12,13]. A potentially more efficient approach may be possible via the electrostatic control of perpendicular magnetic anisotropy (PMA) [14–17]. This effect has been demonstrated in the numerous realizations of magnetoelectric heterostructures based on the FMs, providing a highly potent means to achieve magnetization rotation without involving any electrical current (see, for instance, Refs. [18,19] as well as references therein).

In this work, we theoretically explore the feasibility of PMA-mediated switching between the two quasistable states in the AFMs. The investigation is based on a monodomain model of two compensated magnetic sublattices in the Lagrangian approach. The main focus is on elucidating the basic physical principles of the currentless Néel vector rotation rather than an analysis of a particular implementation, as there can be a wide range of possibilities in the actual realization of the electrically controlled PMA [18–21]. For one, the strain may be used to affect the AFM anisotropy in analogy to FMs. The calculation clearly illustrates the desired AFM reversal by the temporal modulation of the PMA. Further, a detailed analysis reveals magnetization dynamics that are significantly different from those of their FM counterparts, enabling much faster and energy-efficient switching.

II. AFM DYNAMICS UNDER PMA

The process under consideration is akin to dynamical spin reversal, which is a well-established procedure in the spin-echo experiment via a π pulse in the rotating frame of reference [22]. Interestingly, a similar concept has been extended to switch the nanomagnets [23,24]. For a FM, applying the PMA along the z axis [$K_a(t)$] in the form of a single pulse can induce the effective field $\mathbf{H}_{\mathrm{eff}} = -\hat{\mathbf{z}}m_z 2K_a(t)/|\mathbf{M}|$, exerting a torque to rotate $\mathbf{M}$ ($\mathbf{m} = \mathbf{M}/|\mathbf{M}|$) on the x-y plane normal to the PMA [the blue curve in Fig. 1(a)] provided that its strength can overcome the in-plane axial anisotropy (for instance, along the y axis). Unlike magnetic resonance, $\mathbf{H}_{\mathrm{eff}}$ depends on the instantaneous state of $\mathbf{M}$, as shown above. Accordingly, the magnetization executes a flip under the condition $\gamma \int |\mathbf{H}_{\mathrm{eff}}|dt \simeq \pi$, where γ is the gyromagnetic ratio, and approximate conservation of m_z is assumed for the pulse duration. The nonzero m_z needed for magnetization switching can be induced by a weak external magnetic field [24]. Alternatively, the naturally occurring thermal broadening around the equilibrium state (e.g., $m_x = \pm 1, m_z = 0$) can provide the necessary component at sufficiently high temperatures [25].

At first glance, a corresponding effect of PMA-induced reversal seems to be infeasible in AFMs since the effective fields cannot drive the characteristic Néel vector $\mathbf{L}$ to precess
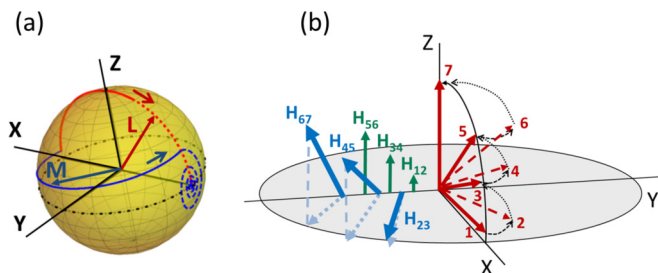
---

*kwk@ncsu.edu

FIG. 1. (a) Schematic illustration of the FM and AFM magnetization vector trajectories (**M** and **L**, respectively) in the reversal motion triggered by a PMA-mediated effective field pulse. For convenience, both **M** and **L** are shown in the normalized form. The key difference is that the FM vector rotates around the equatorial path on the x-y plane (blue), while the AFM counterpart takes the trace on the x-z plane (red) avoiding the hard y axis. The final relaxation to the destination (see the dashed curves) after the PMA pulse is terminated can be achieved much more rapidly in the AFM without the precessional motion. (b) Conceptual depiction of the interplay between the PMA effective field (green arrows) and the exchange field (blue arrows) on the sublattice magnetization $\mathbf{M}_A$ (red arrows). As shown, $\mathbf{M}_A$ evolves from $\mathbf{M}_1$ through $\mathbf{M}_7$ in successive precessions around the corresponding PMA field ($1 \to 2, 3 \to 4, 5 \to 6$ via $\mathbf{H}_{12}, \mathbf{H}_{34}, \mathbf{H}_{56}$) as well as the rotations by the resulting exchange field to restore antiparallel alignment between $\mathbf{M}_A$ and $\mathbf{M}_B$ ($2 \to 3, 4 \to 5, 6 \to 7$ via $\mathbf{H}_{23}, \mathbf{H}_{45}, \mathbf{H}_{67}$). The red contour indicates the ideal-case trajectory with infinitesimal steps. The conjugate dynamics of $\mathbf{M}_B$ are not shown for simplicity.

around it. To illustrate this statement, let us consider an AFM with two sublattices whose magnetizations $\mathbf{M}_A$ and $\mathbf{M}_B$ have an antiparallel orientation at the equilibrium state, i.e., $\mathbf{M}_B = -\mathbf{M}_A$ and $\mathbf{L} = 2\mathbf{M}_A$. When the PMA is applied, one could conclude that precisely antiparallel effective magnetic fields would arise at each sublattice since a strong AFM exchange interaction supposes $m_{B,z} = -m_{A,z}$ at the initial state. The resulting torques on A and B sublattices compensate each other, preventing their rotation on the x-y plane while maintaining the AFM alignment.

However, even a weak asymmetrical perturbation can lift the reversal symmetry between $\mathbf{M}_A$ and $\mathbf{M}_B$, producing fast mutual precession in the exchange fields that are no longer collinear to the respective sublattice magnetization. At the introduction of the PMA, two gyration axes (and thus the sublattice magnetizations) quickly adjust toward the bistable energy minima along the z direction while maintaining nearly antiparallel orientation via strong AFM coupling. Hence, $\mathbf{M}_A$ and $\mathbf{M}_B$ are energetically favored to precess in the different ($\pm z$) hemispheres. A more detailed pictorial description of this process is provided in Fig. 1(b), where the time evolution of the magnetization trajectories is traced by considering the interplay of the PMA effective field and the exchange field. Once the PMA along the z axis is turned on, the sublattice magnetizations initially with $\mathbf{M}_A = \mathbf{M}_1$ and $\mathbf{M}_B = -\mathbf{M}_1$ start to reorient on the x-y plane toward the $+y$ direction, acquiring the same y components for both sublattices ($\mathbf{M}_A = \mathbf{M}_1 \to \mathbf{M}_2$). This breaks their antiparallelism; the resulting exchange fields (e.g., $\mathbf{H}_{23}$) exert mutual rotations of $\mathbf{M}_A$ and $\mathbf{M}_B$ to restore (but not perfectly) the antiparallel alignment by

shifting or buckling the $m_{A,z}$ and $m_{B,z}$ components further in the opposite ($\pm z$) directions (e.g., $\mathbf{M}_A = \mathbf{M}_2 \to \mathbf{M}_3$). The actual trajectory is determined as the aggregate of infinitesimal horizontal rotations (the PMA effect) and vertical motions (the exchange field). The dominant exchange field keeps the magnetization vectors essentially on the x-z plane [see the red solid curve in Fig. 1(b), $\mathbf{M}_1 \to \mathbf{M}_7$].

While the above picture may be overly simplistic, it nevertheless provides a number of valuable insights. The most obvious is that AFM dynamics are determined not only by the PMA-mediated effective field as in FM, but also by the strong interlayer exchange field. As such, the rotation toward the direction of the applied effective field (i.e., the z axis) can occur without explicit involvement of dissipation, unlike in the FMs subjected to precession around it. In fact, strong damping could actually hinder rapid reorientation of the magnetization vectors in the AFMs. Furthermore, the anticipated pendulum-like, semicircular trajectories on the x-z plane suggest the notion of total magnetic energy, thus raising an interesting question about the "kinetic" energy or equivalent in addition to the potential energy corresponding to the anisotropy.

As it turns out, such a degree of freedom is indeed required to describe the AFM dynamics, and it can be expressed in terms of the velocity of the Néel vector $\dot{\mathbf{L}}(t)$ [$\frac{d}{dt}\mathbf{L} = \frac{d}{dt}(\mathbf{M}_A - \mathbf{M}_B)$]. More specifically, the trajectory of the Néel vector is determined not only by its instantaneous position $\mathbf{L}(t)$ (thus, $\mathbf{H}_{\text{eff}}$) but also by the velocity $\dot{\mathbf{L}}(t)$. This means that the vector $\mathbf{L}(t)$ tends to continue its path even after the external driving force is turned off. The underlying implication is that a properly tailored $K_a(t)$, with the aid of the inertial motion, may realize robust or reliable $180°$ inversion between two magnetic energy minima of an AFM [along the $\pm x$ axis; see the red curve in Fig. 1(a)]. Taking into account that the AFM vectors avoid the hard y axis on the equatorial x-y plane, unlike their FM counterparts (e.g., the red versus blue curves), the strength of the PMA required for the switching may be substantially smaller.

III. THEORETICAL MODEL

For a detailed analysis of the PMA-induced AFM dynamics sketched qualitatively above, a monodomain model of two compensated magnetic sublattices is solved by following the Lagrangian formulation developed earlier [26,27]. While the Lagrangian phenomenology can be derived in principle from the microscopic Hamiltonian of localized spin moments with a few additional assumptions [28], we follow the symmetry approach that has been supported by much experimental evidence since its introduction [27]. This treatment conveniently allows the Lagrangian $\mathcal{L}$ to be expressed solely in terms of the AFM Néel vector $\mathbf{L}$ so long as the AFM magnetization $\mathbf{M}$ ($=\mathbf{M}_A + \mathbf{M}_B$), mediated by the misalignment of sublattice magnetizations, is relatively small. Accordingly, the length of the Néel vector $|\mathbf{L}|$ ($=M_L \simeq |\mathbf{M}_A| + |\mathbf{M}_B|$) can be approximately expressed as an integral of motion, and the AFM magnetization acquires a dynamical origin $\mathbf{M} = \frac{H_{\text{ex}}}{\gamma M_L}\mathbf{n} \times \dot{\mathbf{n}}$ at zero magnetic field, where $\mathbf{n} = \mathbf{L}/M_L$, and H_{ex} is the exchange field acting between the sublattices [26,29].

At zero external magnetic field, the Lagrangian

$$\mathfrak{L} = \frac{M_L^2}{2\omega_{\text{ex}}^2}\dot{\mathbf{n}}^2 - W(\mathbf{n}) \tag{1}$$

determines the evolution of the AFM vector. Here, $\omega_{\text{ex}}^2 = \gamma^2 H_{\text{ex}} M_L$, and $W(\mathbf{n})$ is the density of the anisotropy energy, the magnitude of which can be dependent on the shape of the nanomagnet as well as its interfacial characteristics [30]. Combining this inherent contribution with the electrically induced PMA along the z axis, the total anisotropy can be expressed as

$$W(\mathbf{n},t) = \tfrac{1}{2}\left\{K_x n_x^2 + K_y n_y^2 + [K_z + K_a(t)]n_z^2\right\}, \tag{2}$$

where K_x, K_y, and K_z are the values attributed to the structure without external perturbation, and $K_a(t)$ is the electrically mediated PMA, as defined earlier. For simplicity, the cubic and higher-order terms are neglected in Eq. (2). Moreover, K_y can be set to zero without the loss of generality when $\mathbf{n}^2 = 1$; this merely amounts to the renormalization $K_x - K_y \to K_x$ and $K_z - K_y \to K_z$. Then, the magnetic relaxation toward the local minimum of $W(\mathbf{n},t)$ can be incorporated into the kinetic equation by way of a dissipation or damping function,

$$\mathfrak{R} = \frac{\delta_r M_L^2}{2\omega_{\text{ex}}^2}\dot{\mathbf{n}}^2, \tag{3}$$

which can be given in terms of the homogeneous linewidth δ_r of AFM resonance. The correspondent Lagrange equation augmented with the dissipation [Eq. (3)] describes the evolution of the AFM vector in the form of a Langevin second-order differential equation,

$$\mathbf{n} \times \left[\ddot{\mathbf{n}} + \omega_{ex}^2 \frac{\partial}{\partial \mathbf{n}}\frac{W(\mathbf{n},t)}{M_L^2} + \delta_r\dot{\mathbf{n}}\right] = 0. \tag{4}$$

Similar expressions have been obtained earlier except $W(\mathbf{n},t)$, which now explicitly represents the time-dependent PMA [9]. This second-order nature highlights the dependence on the velocity $\frac{d\mathbf{n}}{dt}$ (or $\frac{d}{dt}\mathbf{L}$) mentioned above.

To proceed further, it is convenient to represent Eq. (4) via polar and azimuthal angles of vector $\mathbf{n}(t) = (\sin\theta\cos\varphi, \sin\theta\sin\varphi, \cos\theta)$ and introduce dimensionless time $t \to \omega_r t$ in terms of the zero-field AFM resonance frequency $\omega_r = \gamma\sqrt{2H_{\text{ex}}H_{\text{an}}}$. Here, H_{an} represents the effective anisotropy field $(=|K_x|/\tfrac{1}{2}M_L)$. Then, the corresponding expressions take the form

$$\ddot{\theta} = \sin 2\theta\left[\tfrac{1}{2}\dot{\varphi}^2 + \xi_z + \xi_a(t) - \xi_x\cos\theta\right] - \lambda\dot{\theta}, \tag{5}$$

$$\ddot{\varphi}\sin^2\theta = -\dot{\theta}\dot{\varphi}\sin 2\theta + \xi_x\sin^2\theta\cos 2\varphi - \lambda\dot{\varphi}\sin^2\theta, \tag{6}$$

where $\xi_x = K_x/2|K_x|$, $\xi_z = K_z/2|K_x|$, $\xi_a(t) = K_a(t)/2|K_x|$, and $\lambda = \delta_r/\omega_r$.

To solve these coupled equations, appropriate initial conditions (defined as θ_0, φ_0, $\dot{\theta}_0$, and $\dot{\varphi}_0$ for the respective parameters) need to be specified. Note that the minimum of the AFM anisotropy energy at $t = 0$ (i.e., $\theta_0 = \pi/2$ and $\varphi_0 = 0$) is just one particular realization among the possible configurations at a nonzero temperature T. Similarly, the initial "velocities" $\dot{\theta}_0$ and $\dot{\varphi}_0$ are also distributed according to the "kinetic energy" with a dispersion around the ambient thermal

energy $k_B T$. To account for all of the physically possible $\mathbf{n}(t)$ and $\dot{\mathbf{n}}(t)$, the effect of thermal fluctuation in the initial AFM orientation may need to be considered. The desired distribution $P(\mathbf{q})$ can be introduced in terms of the Hamilton function that represents the total energy E of the AFM with volume V_0 in the phase space $\mathbf{q}$ $[=(\theta,\varphi,\dot{\theta},\dot{\varphi})]$ (i.e., the coordinates of $\mathbf{n}$ and $\dot{\mathbf{n}}$). More specifically, the explicit form for E is obtained directly from the Lagrangian [Eq. (1)] as

$$\frac{E}{V_0} = \dot{\mathbf{n}}\frac{\partial\mathfrak{L}}{\partial\dot{\mathbf{n}}} - \mathfrak{L}. \tag{7}$$

Then one can arrive, after some algebra, at the following:

$$E(\mathbf{q}) = E_M(4\dot{\theta}^2 + 4\dot{\varphi}^2\sin^2\theta + \xi_x\sin^2\theta\cos^2\varphi + \xi_z\cos^2\theta), \tag{8}$$

where $E_M = M_L H_{\text{an}} V_0$. Finally, the usual canonical expression leads to the equilibrium distribution function $P(\mathbf{q}) = N\exp\left[-\frac{E(\mathbf{q})}{k_B T}\right]$ with a normalization factor N, i.e., $\int P(\mathbf{q})d\mathbf{q} = 1$. The range of typical initial conditions can be obtained in terms of the root-mean-square value $\langle\Delta q_i\rangle = \sqrt{\overline{q_i^2}}$, where $\overline{q_i^2} = \int q_i^2 P(\mathbf{q})d\mathbf{q}$. The problem is simplified when the relatively small dispersion $\Delta\mathbf{q}$ $[=(\frac{\pi}{2} - \Delta\theta, \Delta\varphi, \Delta\dot{\theta}, \Delta\dot{\varphi})]$ around the energy extremum $\mathbf{q}_0 = (\frac{\pi}{2},0,0,0)$ is taken into consideration. The estimates give $\langle\Delta\dot{\theta}\rangle = \langle\Delta\dot{\varphi}\rangle = \sqrt{k_B T/8E_M}$, $\langle\Delta\theta\rangle = \sqrt{k_B T/2E_M|\xi_x - \xi_z|}$, and $\langle\Delta\varphi\rangle = \sqrt{k_B T/2E_M\xi_x}$. The increase of dispersion $\langle\Delta\theta\rangle$ with a reduction in the difference $\xi_x - \xi_z$ is not surprising when considering that the x axis ceases to be the easy axis as $\xi_x - \xi_z \to 0$. Then, the x-z plane instead becomes the easy plane with a much broader initial distribution.

IV. RESULTS AND DISCUSSION

Utilizing the formulation described above, the solutions of Eqs. (5) and (6) can be obtained under electrically induced PMA [i.e., $\xi_a(t)$] and initial conditions $\mathbf{q}$ ($t = 0$). For the numerical results, we exploit the simplest case of an easy-axis AFM (assuming $K_x = -2.5 \times 10^5$ erg/cm^3, $K_z = 0$) and adopt the typical AFM zero-field resonance frequency f_r $(=\omega_r/2\pi)$ of 150 GHz along with the sublattice magnetization $M_L/2$ of 200 Oe. These parameters correspond to the effective fields $H_{\text{an}} = 1250$ Oe and $H_{\text{ex}} = 1.1$ MOe according to the simple models considered. The quantity of the magnetic energy E_M is linearly proportional to the volume V_0 (assumed to be $60 \times 60 \times 2$ nm^3) whose magnitude would provide nonvolatility at room temperature ($\approx 40 k_B T$). The PMA applied in the form of a rectangular pulse with amplitude $K_a = -4 \times 10^5$ erg/cm^3 and duration Δt is assumed at $t = 0$, which alters the easy axis to be essentially along the z direction. Thus, the full set of parameters $\xi_x = -0.5$, $\xi_a(t) = -0.8$ [only for $t \in (0,\Delta t)$], and the damping factor $\lambda = 0.4$ determines the Néel vector evolution in terms of the expressions given above and the dimensionless time $\omega_r t$. The corresponding broadening around the energy minimum $E(\mathbf{q}_0)$ is estimated to be $\langle\Delta\varphi\rangle \simeq \langle\Delta\theta\rangle \simeq 5°$, $\langle\Delta\dot{\theta}\rangle \simeq \langle\Delta\dot{\varphi}\rangle \simeq 0.06$ at room temperature, which is used to determine the typical initial conditions of the AFM magnetization accounting for the effect of thermal fluctuations. An alternative
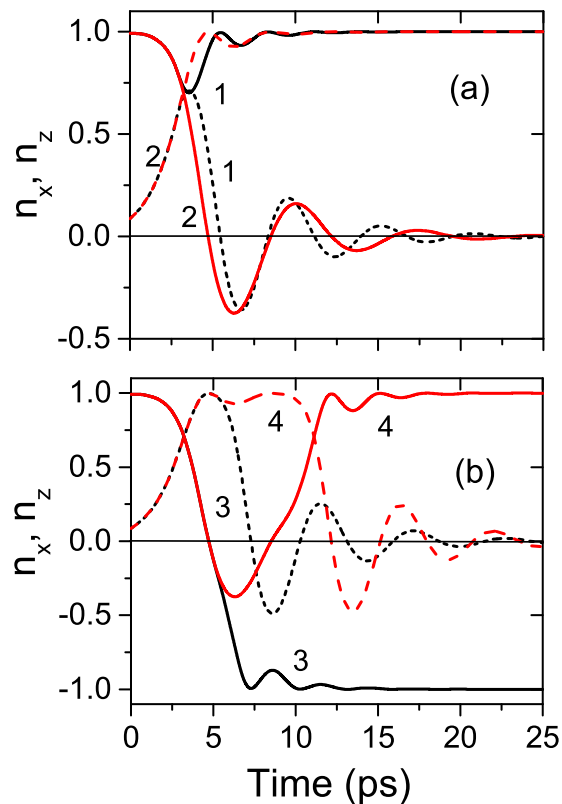
FIG. 2. Temporal evolution of the AFM Néel vector **n** (=**L**/|**L**|) under a PMA-mediated effective field with different pulse durations Δt; (a) 3 ps (curve 1), >25 ps (curve 2) and (b) 6 ps (curve 3), 9 ps (curve 4). The solid lines show the x component (n_x), while the dashed lines are for the z component (n_z). Due to the hard y axis, the motion in this direction (n_y) is rather insignificant and thus not shown. The calculations are based on the Lagrangian approach [Eqs. (5) and (6)] with the initial state of the Néel vector slightly canted from the equilibrium orientation (i.e., $\theta = 85°, \varphi = 5°, \dot\theta = \dot\varphi = 0.06$).
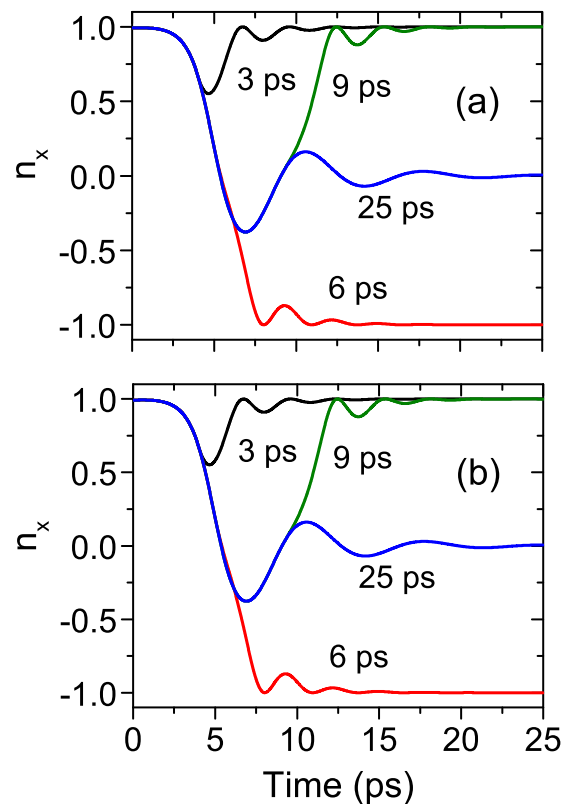

FIG. 3. Comparison of the Néel vector dynamics obtained with (a) the micromagnetic LLG simulation and (b) the present Lagrangian monodomain approach. Unlike in Fig. 2, the initial velocity of the Néel vector is set to zero in the Lagrangian approach to be consistent with the LLG treatment.

approach, on the other hand, requires repetitive sampling over the four-dimensional parameter space **q** [According to the distribution function $P(\mathbf{q})$] with sufficiently fine coverage. As the current analysis is focused on the prevalent behaviors of the system rather than the deviation from the norm, the adopted treatment utilizing the likely initial state is expected to adequately describe the AFM response to the applied PMA at finite temperature. A detailed examination of thermal variation/noise in the switching dynamics is beyond the scope of this investigation.

Figure 2 shows the results of AFM dynamics simulation for four different values of pulse duration Δt. Following the discussion given above, the initial state of the Néel vector is chosen slightly away from the equilibrium orientation along with the nonzero velocities to account for the thermal broadening (i.e., $\theta = 85°, \varphi = 5°, \dot\theta = \dot\varphi = 0.06$). As shown in Fig. 2(a), the cases in either extreme of Δt can be readily understood. The Néel vector aligns, after some oscillations, along the z axis with a long PMA pulse (thus, a 90° rotation; curve 2), while an insufficient duration leads to the relaxation back to the initial orientation, as expected (e.g., $\Delta t = 3$ ps; curve 1). In comparison, the outcome of the

dynamics is seemingly more complex in the intermediate regime [Fig. 2(b)]. Here, a shorter pulse leads to the 180° flip as desired (6 ps; curve 3), whereas a somewhat longer pulse is predicted with a botched reversal resulting in an about-face instead (9 ps; curve 4). The clue for this behavior can actually be found from the temporal dynamics under a long pulse shown in Fig. 2(a). At $t = 6$ ps, the Néel vector has passed the potential minimum at $n_z = 1, n_x = 0$ and is moving toward the $n_x = -1$ direction. On the other hand, time $t = 9$ ps is after the Néel vector has changed the trajectory and is now heading to the positive n_x territory. Thus, the "moment of inertia" at the time when the PMA pulse is cut off appears to be crucial near the $n_z = 0$ point (i.e., the potential apex without the PMA) in determining the final resting place ($n_x = +1$ or -1) in the subsequent AFM relaxation. These dynamics indeed resemble a pendulum-like back-and-forth oscillation on the x-z easy plane instead of the FM-like precession around the z axis, confirming the qualitative picture provided earlier (Fig. 1). Accordingly, the desired 180° reversal can be realized deterministically by optimizing the PMA pulse duration. The window of operation for Δt is also expected to be cyclic when considering the oscillatory dynamics pattern.

For validation of the results, it is interesting to compare the AFM dynamics predicated by the present approach with those of micromagnetic simulation, as shown in Fig. 3. In the latter treatment [31], an AFM is considered as the foliated FM
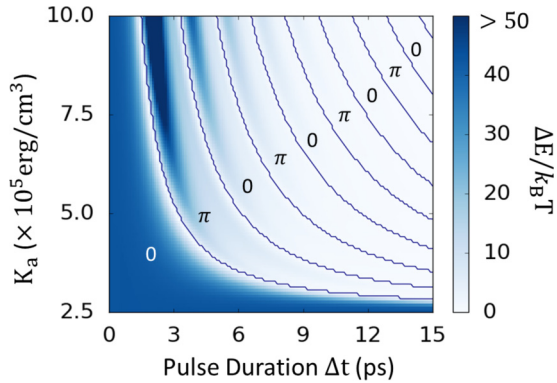
FIG. 4. Phase diagram of the AFM response in terms of the pulse duration and the amplitude. The regions with "0" and "π" represent the conditions resulting in the final Néel vector state of $n_x = 1$ (no change) and $n_x = -1$ (reversal), respectively. The color map illustrates the stability of the switching response, where ΔE denotes the estimated energy barrier against a completely random thermal outcome. The darker color corresponds to higher fidelity in the predicted result.

layers with AFM interactions between them. In turn, each FM layer consists of small FM cells driven by local exchange fields according to the Landau-Lifshitz-Gilbert (LLG) equation [32]. In this calculation, we choose the FM cell sizes of $0.5 \times 0.5 \times 0.5$ nm^3 with the cube face area $A_c = 0.25$ nm^2. In addition, the required interlayer (intralayer) exchange constants are set at $J = -(+)5 \times 10^{-7}$ erg/cm, which, according to an approximate expression $|J| = \frac{1}{2} M_L H_{ex} A_c$, matches well with the AFM exchange field estimate discussed above in the Néel vector description ($H_{ex} = 1.1$ MOe). The numerical values for the characteristic parameters (such as V_0, K_x, M_L, K_a, and λ) also remain the same, which give the Gilbert damping constant $\alpha = \lambda \sqrt{H_{an}/H_{ex}} = 0.01$ and the zero-field resonance frequency of around 150 GHz. One additional provision is that the magnetization in each FM layer at $t = 0$ (i.e., the initial condition) is canted slightly (e.g., $\mp 5°$) from the minimum state of $m_x = \pm 1$ with net zero total magnetization to mimic the thermal broadening effect discussed earlier. The corresponding conditions for the Néel vector model are $\theta = 85°$, $\varphi = 5°$, $\dot{\theta} = 0$, and $\dot{\varphi} = 0$, for which the initial velocity is set to zero (i.e., $\dot{\mathbf{L}} = \mathbf{0}$ at $t = 0$). This is to be consistent with the LLG treatment (that contains no such dependence) and thus differs from those used in Fig. 2. The simulation results clearly illustrate that both approaches predict essentially the identical responses in the AFM dynamics despite the major differences in the underlying assumptions. Even the noncoherent dynamics of the FM cells in the micromagnetic simulation consistently indicate the fast,

pendulum-like switching of the magnetization vectors in the AFMs, avoiding the hard y axis.

With the feasibility of the phenomenon illustrated as described above, we examine in greater detail the conditions necessary for the successful PMA-induced reversal. Figure 4 provides a correspondent phase diagram of the AFM response in terms of the pulse duration and the amplitude. The alternating property of the phase diagram in Δt confirms the cyclic behavior of the pendulum-like AFM dynamics mentioned earlier. However, the cases with a long Δt may become unstable at high temperatures. As illustrated by curve 2 in Fig. 2(a), the damped oscillation experienced at large t is indicative of the diminished "kinetic energy." Accordingly, the random thermal fluctuations can wield a larger influence than the inertial motion in the relaxation process that follows the termination of the PMA pulse (see the color map in Fig. 4). Other adjustments heretofore undiscussed will also be needed to accommodate the properties of a specific AFM in the actual implementation. Nevertheless, the pendulum-like AFM dynamics are expected to provide a robust switching mechanism under a properly tailored PMA pulse. In particular, the dark colored regions of the phase space with a large energy barrier ΔE (against the random thermal motions) can ensure the desired dynamical response with high fidelity. This tends to require a strong PMA and a relatively short Δt. The large barrier can also alleviate the impact of the initial state variation discussed earlier.

V. SUMMARY

In this work, an effective mechanism of AFM switching is illustrated. In contrast to the spin-transfer torque [5,8,9], the PMA-mediated Néel vector reversal occurs with an electrostatic field and does not require an electrical current. Accordingly, the energy consumption for a single device operation can be expected in the range of a few aJ [33]. As for electrical detection, the giant magnetoresistance effect in a heterostructure with a FM of fixed magnetization may provide a solution [1,2]. Alternatively, one may utilize the surface conductance of a topological insulator that is sensitive to the magnetization direction of the proximate AFM sublattice at the interface. Apart from evident application to low-power memory [34], the strong nonlinearity of the response to an input signal may also enable logic functions with speed and energy efficiency.

[1] M. N. Baibich, J. M. Broto, A. Fert, F. Nguyen Van Dau, F. Petroff, P. Etienne, G. Creuzet, A. Friederich, and J. Chazelas, Phys. Rev. Lett. **61**, 2472 (1988).

[2] S. S. P. Parkin, N. More, and K. P. Roche, Phys. Rev. Lett. **64**, 2304 (1990).

[3] E. V. Gomonay and V. M. Loktev, Low Temp. Phys. **40**, 17 (2014).

[4] T. Jungwirth, X. Marti, P. Wadley, and J. Wunderlich, Nat. Nanotechnol. **11**, 231 (2016).

[5] R. Cheng, M. W. Daniels, J.-G. Zhu, and D. Xiao, Phys. Rev. B **91**, 064423 (2015).

[6] S. Fukami, C. Zhang, S. Dutta Gupta, A. Kurenkov, and H. Ohno, Nat. Mater. **15**, 535 (2016).

[7] Y.-W. Oh, S. C. Baek, Y. M. Kim, H. Y. Lee, K.-D. Lee, C.-G. Yang, E.-S. Park, K.-S. Lee, K.-W. Kim, G. Go, J.-R. Jeong, B.-C. Min, H.-W. Lee, K.-J. Lee, and B.-G. Park, Nat. Nanotechnol. **11**, 878 (2016).

[8] A. S. Núñez, R. A. Duine, P. Haney, and A. H. MacDonald, Phys. Rev. B **73**, 214426 (2006).

[9] H. V. Gomonay and V. M. Loktev, Phys. Rev. B **81**, 144427 (2010).

[10] P. Wadley, B. Howells, J. Zelezný, C. Andrews, V. Hills, R. P. Campion, V. Novák, K. Olejník, F. Maccherozzi, S. S. Dhesi, S. Y. Martin, T. Wagner, J. Wunderlich, F. Freimuth, Y. Mokrousov, J. Kuneš, J. S. Chauhan, M. J. Grzybowski, A. W. Rushforth, K. W. Edmonds, B. L. Gallagher, and T. Jungwirth, Science **351**, 587 (2016).

[11] J. C. Slonczewski, J. Magn. Magn. Mater. **159**, L1 (1996).

[12] T. Shiino, S.-H. Oh, P. M. Haney, S.-W. Lee, G. Go, B.-G. Park, and K.-J. Lee, Phys. Rev. Lett. **117**, 087203 (2016).

[13] P. E. Roy, R. M. Otxoa, and J. Wunderlich, Phys. Rev. B **94**, 014439 (2016).

[14] M. Weisheit, S. Fähler, A. Marty, Y. Souche, C. Poinsignon, and D. Givord, Science **315**, 349 (2007).

[15] T. Maruyama, Y. Shiota, T. Nozaki, K. Ohta, N. Toda, M. Mizuguchi, A. A. Tulapurkar, T. Shinjo, M. Shiraishi, S. Mizukami, Y. Ando, and Y. Suzuki, Nat. Nanotechnol. **4**, 158 (2009).

[16] Y. Shiota, T. Nozaki, F. Bonell, S. Murakami, T. Shinjo, and Y. Suzuki, Nat. Mater. **11**, 39 (2012).

[17] W.-G. Wang, M. Li, S. Hageman, and C. L. Chien, Nat. Mater. **11**, 64 (2012).

[18] C. A. F. Vaz, J. Phys.: Condens. Matter **24**, 333201 (2012).

[19] Y. Hibino, T. Koyama, A. Obinata, K. Miwa, S. Ono, and D. Chiba, Appl. Phys. Exp. **8**, 113002 (2015).

[20] K. Roy, S. Bandyopadhyay, and J. Atulasimha, Appl. Phys. Lett. **99**, 063108 (2011).

[21] Y. G. Semenov, X. Duan, and K. W. Kim, Phys. Rev. B **86**, 161406(R) (2012).

[22] A. Abragam, *The Principles of Nuclear Magnetism* (Oxford University Press, New York, 1961), Chap. 3.

[23] X. Li, D. Carka, C. Liang, A. E. Sepulveda, S. M. Keller, P. K. Amiri, G. P. Carman, and C. S. Lynch, J. Appl. Phys. **118**, 014101 (2015).

[24] C. Grezes, F. Ebrahimi, J. G. Alzate, X. Cai, J. A. Katine, J. Langer, B. Ocker, P. Khalili Amiri, and K. L. Wang, Appl. Phys. Lett. **108**, 012403 (2016).

[25] D. V. Berkov, IEEE Trans. Magn. **38**, 2489 (2002).

[26] I. V. Bar'yakhtar and B. A. Ivanov, Fiz. Nizk. Temp. **5**, 759 (1979) [Sov. J. Low Temp. Phys. **5**, 361 (1979)].

[27] A. F. Andreev and V. I. Marchenko, Sov. Phys. Usp. **23**, 21 (1980).

[28] B. A. Ivanov, Low Temp. Phys. **31**, 635 (2005).

[29] I. V. Bar'yakhtar and B. A. Ivanov, Solid State Commun. **34**, 545 (1980).

[30] O. Gomonay, S. Kondovych, and V. Loktev, J. Magn. Magn. Mater. **354**, 125 (2014).

[31] M. J. Donahue and D. G. Porter, OOMMF User's Guide, Version 1.0 (NIST, Gaithersburg, MD, 1999).

[32] I. Cimrák, Arch. Comput. Methods Eng. **15**, 277 (2008).

[33] X. Duan, Y. G. Semenov, and K. W. Kim, Phys. Rev. Appl. **2**, 044003 (2014).

[34] K. Galatsis, K. Wang, Y. Botros, Y. Yang, Y.-H. Xie, J. F. Stoddart, R. B. Kaner, C. Ozkan, J. Liu, M. Ozkan, C. Zhou, and K. W. Kim, IEEE Circ. Dev. Mag. **22**, 12 (2006).